

Simultaneous layout and topology optimization of curved stiffened panels

Sheng Chu¹, Scott Townsend² and Carol Featherston³
School of Engineering, Cardiff University, Cardiff, CF24 3AA, United Kingdom

H. Alicia Kim⁴
Structural Engineering Department, University of California San Diego, CA 92093, USA

Simultaneous layout and topology optimization of stiffened panels is investigated in this paper using a new level-set-based method. Specifically, plate elements are used to construct a stiffened panel structure. The level set method is then used to manipulate the stiffener layout, with curved members allowed. A free-form mesh deformation method with a control mesh is utilized to adjust the finite element mesh. The level set method is also used to optimize the internal topologies of the stiffeners. Both mass minimization with buckling constraint and critical buckling load factor maximization with mass constraint are investigated. A semi-analytical sensitivity analysis is performed, and the optimization algorithm is outlined. For the buckling-constrained problem, the p -norm function is used to aggregate multiple buckling modes and a gradient-based optimizer is used with an adaptive scaling method to enforce exact control of the buckling limit. Numerical investigations demonstrate and validate the proposed method.

Nomenclature

A_{\min}	=	lower bound of element distortion constraints
A_r	=	r th element distortion constraint
E	=	Young's modulus
\mathbf{f}	=	applied load

¹ PhD student, School of Engineering, AIAA student member.

² Research associate, School of Engineering.

³ Professor, School of Engineering.

⁴ Professor, Structural Engineering Department, AIAA associate fellow.

g = general function
 K = elemental stiffness matrix
 \mathbf{K} = structural stiffness matrix
 K_g = elemental geometric stiffness matrix
 \mathbf{K}_g = structural geometric stiffness matrix
 L_l = l th stiffener spacing constraint
 L_{\min} = lower bound of stiffener spacing constraints
 L^{pf-1}, L^{pf} = lengths of the elemental boundaries with the node pf
 m = structural mass
 m_{\max} = upper bound of the structural mass
 M_p = p -norm function
 N = number of stiffeners
 \mathbf{N} = shape function
 N_L = number of stiffener spacing constraints
 N_A = number of element distortion constraints
 N_λ = number of buckling modes considered in the optimization
 p = aggregation parameter
 P = pressure value per unit length
 P_{pf} = force applied on the node pf
 $\mathbf{r}_x, \mathbf{r}_y, \mathbf{r}_z$ = rotations
 t = thickness
 t_f = fictitious time
 \mathbf{u} = stationary deflection
 \mathbf{u}_{ad} = adjoint vector
 v = volume fraction
 \mathbf{v} = eigenvector
 V = velocity vector
 V_n = normal velocity

w = physical density
 \mathbf{w} = physical density distribution
 $\mathbf{u}, \mathbf{v}, \mathbf{w}$ = translational displacements
 x = coordinate used in the level set mesh coordinate system
 $\mathbf{x}_{control}$ = nodal coordinate on the control mesh
 \mathbf{x}_{FE} = nodal coordinate on the FE mesh
 \mathbf{y} = change in the coordinates of the control mesh nodes
 \mathbf{z} = change in the coordinates of the FE mesh nodes
 Γ = boundary of design domain
 Φ = level set function
 Ω = domain containing the structure
 Ω_d = design domain
 α_1, α_2 = adaptive scaling factors
 γ_1, γ_2 = move limits
 λ = buckling load factor
 λ_1 = critical buckling load factor
 λ_{min} = lower bound of the critical buckling load factor
 μ = inverse of the buckling load factor
 ρ = mass density
 ν = Poisson's ratio

Subscripts

b = structural boundary
 i = index of the nodal coordinate of the control mesh
 j = index of the finite element
 l = layout of stiffeners
 pl = index of the discrete point
 q = index of the buckling mode
 s = solid phase

t_0 = index of level set function representing internal topology of the stiffener

v = void phase

0 = current iteration

Superscripts

k = iteration number

pf = index of the node on the FE mesh

s = solid phase

v = void phase

I. Introduction

As one of the primary structural configurations in an aircraft, stiffened panels are ubiquitous and play an important role in aerospace structures. To improve their strength to weight ratios and make them cost-effective, they are generally designed for maximum strength, stiffness and buckling performance, or for minimum weight whilst maintaining constraints on buckling and stress.

Since Bedair [1] investigated the effect of stiffener location on structural stability noting that the size of a stiffener influences its optimal location, many research works for the optimum design of stiffened panels have been conducted within the frameworks of size and layout optimization [2-8], to determine the best thickness distribution, orientation, spacing and placement of stiffeners, as well as the optimal curvature for curved stiffeners. In these frameworks, one notable trend is the application of gradient-free optimization techniques such as Genetic Algorithms (GAs), Particle Swarm Optimization (PSO), and Response Surface Approaches (RSA). Though these optimization problems can be effectively solved using gradient-free optimization techniques, this family of algorithms is computationally expensive and scales very poorly with the number of design variables. To alleviate these issues, Stanford et al. [9] developed a nested optimization to simultaneously handle wingbox rib and skin stiffener layout design with a mixed-integer surrogate infill optimizer, as well as a spatially detailed set of component sizing design variables with a gradient-based sizing optimizer. The optimization of the stiffener number was also considered.

Many attempts have been made to improve the structural performance of stiffened panels; however, their design within the frameworks of size and layout optimization is always conducted under the assumption that the internal topology of each stiffener is predetermined. Unlike these size and shape optimizations, topology optimization can be

conducted at the concept design stage where information on structural geometry and topology are unknown. In this way it is able to achieve the structure with the optimal performance by adding, removing and redistributing materials. Since the pioneering work of Bendsøe and Kikuchi [10], different topology optimization methods, such as the solid isotropic material with penalization (SIMP) method [11-13], the level set method (LSM) [14-17] and the evolutionary approach [18, 19] have been developed. Some of these have been applied to buckling problems [20-23]. Among these works, two main issues are always discussed. The first is related to the spurious buckling loads or load factors being generated by the finite element analysis (FEA), due to low-density regions. To address this issue, different interpolation schemes for the stiffness and geometric stiffness matrices [20, 22, 24] have been explored for both the SIMP and level-set-based methods, and an approach based on the eigenvalue shift and pseudo mode identification [22] has been suggested. The other main issue identified is related to convergence [25] and is generally caused by inaccurate sensitivity information on critical buckling loads or load factors, for example due the influence of the variation of the stress state and the non-differentiability of the multiple eigenvalues being neglected. Switching of the critical buckling mode during optimization can also be a source of convergence problems. During optimization, the buckling mode with the lowest load factor may change. Therefore, the mode shape and gradient information relating to the lowest buckling mode change, resulting in a discontinuous and slow convergence. To improve the convergence, a simple strategy is to consider a large number of buckling modes in optimization. However, this will significantly increase the computational cost. As well as this, when the buckling performance is considered in the constraints, the number of constraints is increased. To reduce the buckling constraints, the p -norm and KS functions are used in Dienemann et al. [26], Stanford et al. [9], and Ferrari and Sigmund [27]. For the topological design of stiffened panels, Stanford et al. [28] and Townsend and Kim [24] used SIMP-based and level-set-based approaches respectively, to optimize the internal topology of each stiffener. However, both of these works were conducted based on predetermined structural thickness distributions and stiffener layouts.

Until now, the design of stiffened panels simultaneously optimizing the layout and internal topologies of the stiffeners has not been investigated. The main reason for this is that one cannot expect a reliable convergence when applying gradient-free optimization approaches to this optimization problem due to the large number of design variables in topology optimization. Meanwhile, there is still no effective gradient-based optimization method to handle the layout optimization.

It is noted that, in contrast to traditional panels stiffened with straight stiffeners, Kapania et al. [3] introduced curvilinearly stiffened panels and showed that they have the potential to result in lighter weight designs. Continuing this research on curvilinearly stiffened panels, they developed a framework, EBF3PanelOpt, for their design optimization [6, 7, 29]. In these works however, stiffener curves are limited by pre-specified curvilinear functions, e.g. third order uniform rational B-spline, as well as the optimization design space.

The level set method has attracted lots of attention, particularly in the fields of image processing, interface motion tracking and topology optimization [15, 30, 31]. Its ability to describe variations in topology, increases the design space with the potential to find the global optimum in optimization problems.

This paper proposes a new level-set-based method to simultaneously conduct the layout and topology optimization of curved stiffened panels. For the layout optimization, the level set function (LSF) is used to describe and freely manipulate the stiffener curves. To achieve this the stiffened panel is discretized into plate elements. To avoid re-meshing during optimization, the free-form mesh deformation method with control mesh is developed to adjust the finite element (FE) mesh after every update of the stiffener layout. The level set method is also used for the internal topology optimization of the stiffeners, with each stiffener represented by one LSF. Both the problems of mass minimization with buckling constraint and critical buckling load factor maximization with mass constraint are investigated. A semi-analytical sensitivity analysis is performed, and the gradient-based optimizer IPOPT [32] is used. For the buckling-constrained problem, when the p -norm function and IPOPT are used, an adaptive scaling method is used to ensure the control of the buckling limit. The effectiveness of the proposed method is shown through its applications to the two problems.

The remainder of this paper is organized as follows. In Section 2, the geometry and FE models of curved stiffened panels are presented. Section 3 describes the mathematical formulations of the considered problems, sensitivity analysis and optimization algorithm. Some numerical examples to test the proposed method are presented in Section 4. Conclusions are given in Section 5.

II. Curved Stiffened Panel Model

In this section, the geometry and FE models are described. LSFs are used to represent and optimize both the layout and the internal topologies of the stiffeners. As the stiffener layout changes, a free-form mesh deformation method with a control mesh is used to adjust the FE mesh.

A. Stiffener Layout

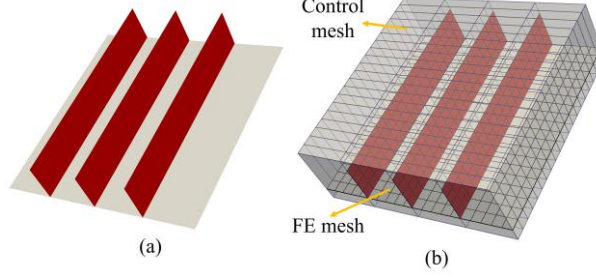


Fig. 1: Sample curved stiffened panel and its control and FE meshes: (a) geometry model; (b) control and FE meshes.

The stiffened panel is composed of the skin and stiffeners shown in Fig. 1(a). The level set method [14, 15, 17] is used to represent and manipulate the layout of the stiffeners, allowing curved members. Specifically, as shown in Figs. 2(a) and 2(d), the stiffener curves are defined as the zero level set of an implicit function:

$$\Phi_l(x_l) = 0 \quad x_l \in \Gamma_l \quad (1)$$

where Γ_l denotes the stiffener curves. $\Phi_l(x_l)$ is the implicit function and $x_l \in \Omega_{d,l}$, where $\Omega_{d,l}$ is the design domain corresponding to the panel. Conventionally, the signed distance function is used for the LSF.

To achieve the optimal layout of the stiffeners, the stiffener curves are optimized by iteratively solving the level set equation, Eq. (2)

$$\frac{\partial \Phi_l(x_l, t_f)}{\partial t_f} + \nabla \Phi_l(x_l) \cdot V_l(x_l) = 0 \quad (2)$$

where t_f is a fictitious time and V_l is the velocity vector.

The LSF at each point is updated by solving the following discretized Hamilton-Jacobi equation using an up-wind differential scheme [30],

$$\Phi_{l,pl}^{k+1} = \Phi_{l,pl}^k - \Delta t_f \left| \nabla \Phi_{l,pl}^k \right| V_{n,l,pl} \quad (3)$$

where $V_{n,l}$ is the normal velocity. pl is a discrete point in the design domain, k is the iteration number and $|\nabla \Phi_{l,pl}^k|$ is computed for each point using the Hamilton-Jacobi weighted essentially non-oscillatory method (HJ-WENO) [33].

To improve the computational efficiency, the level set update is restricted to points within a narrow band close to the boundary in this work. We choose $\Phi_{l,pl}$ to be a signed distance to the boundary only within this narrow band. To correct for this effect, $\Phi_{l,pl}$ is periodically reinitialized to a signed distance function. The fast-marching method [30] is used for this re-initialization and velocity extension.

In this work, both the skin and stiffeners are modeled explicitly with 4-node Mixed Interpolation of Tensorial Components (MITC) plate elements with 6 DOF's per node, comprising a Mindlin-Reissner plate element [34, 35] combined with the plane stress formulation. In order to avoid re-meshing after every update of the stiffener layout, the free-form mesh deformation method with control mesh is developed. In Fig. 1(b), the control mesh, represented by the blue lines and grey surfaces is generated. The intermediate elemental surfaces correspond to the stiffeners, which means that the coordinates in the x and y directions of nodes on the control mesh are all located on the stiffener curves represented by the zero level set in Eq. (1). As the LSF is updated from Fig. 2(a) to Fig. 2(d), the nodes on the control mesh are re-located from Fig. 2(b) to Fig. 2(e). For simplification of implementation, the y and z coordinates of the nodes on the control mesh are fixed and only the x coordinates are allowed to move. Using the free-form mesh deformation method [36], as shown in Figs. 2(c) and 2(f), the FE mesh is deformed to cater to the updated stiffener layout with control mesh:

$$\mathbf{x}_{FE} = \mathbf{N}\mathbf{x}_{control} \quad (4a)$$

$$\mathbf{x}_{control}^{k+1} = \mathbf{x}_{control}^k + \mathbf{y} \quad (4b)$$

$$\mathbf{x}_{FE}^{k+1} = \mathbf{x}_{FE}^k + \mathbf{z} \quad (4c)$$

$$\mathbf{z} = \mathbf{N}\mathbf{y} \quad (4d)$$

where \mathbf{x}_{FE} and $\mathbf{x}_{control}$ are nodal coordinates on the FE and control meshes, respectively. \mathbf{N} is the shape function. \mathbf{y} and \mathbf{z} represent the changes in the coordinates of the control and FE mesh nodes, respectively. The deformation of the FE mesh can be achieved through Eqs. (4c) and (4d).

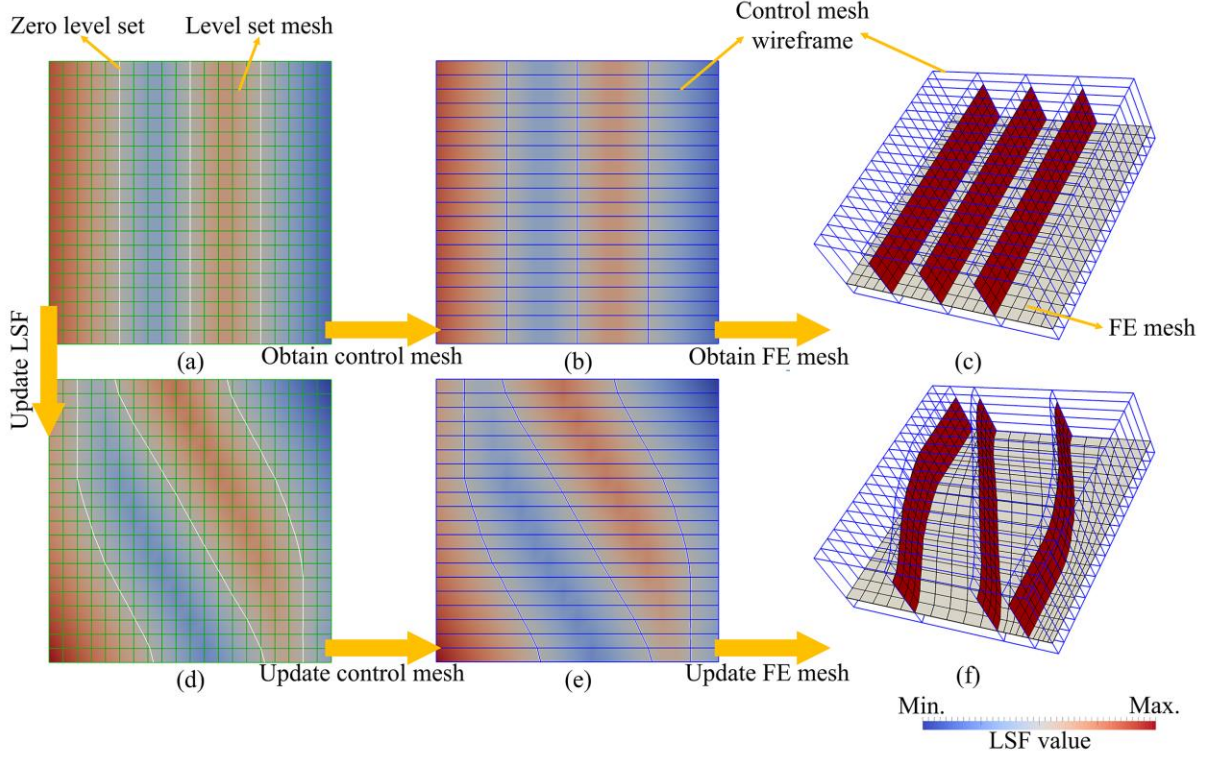


Fig. 2: Illustration of the curved stiffener layout represented by the LSF, with white, green, blue and black lines representing the zero level set, the level set mesh, the control mesh wireframe and the FE mesh respectively: (a) the LSF, the zero level set and the level set mesh for the initial structure; (b) the LSF, the zero level set and the control mesh wireframe for the initial structure; (c) the initial control mesh wireframe and the FE mesh; (d) the LSF, the zero level set and the level set mesh for the updated structure; (e) the LSF, the zero level set and the control mesh wireframe for the updated structure; (f) the updated control mesh wireframe and the FE mesh.

B. Stiffener Internal Topology

The level set method is also used to represent and optimize the internal topologies of the stiffeners with one LSF used to describe the internal topology of each stiffener. The relationship between the LSF values and the resulting structures are shown in Figs. 3(b)-3(d). The structural boundary is defined as the zero level set of the implicit function

$\Phi_{to}(x_{to})$:

$$\begin{cases} \Phi_{to}(x_{to}) \leq 0 & x \in \Omega_{to} \\ \Phi_{to}(x_{to}) = 0 & x \in \Gamma_{to} \\ \Phi_{to}(x_{to}) > 0 & x \notin \Omega_{to} \end{cases}, \quad to = 1, 2, \dots, N \quad (5)$$

where Φ_{to} is the LSF representing the to -th stiffener, and N is the number of stiffeners. For the to -th stiffener, Ω_{to} is the domain corresponding to the structure and Γ_{to} is the structural boundary. $x \in \Omega_{d,to}$, where $\Omega_{d,to}$ is the design domain

containing the structure, $\Omega_{to} \in \Omega_{d,to}$. As in Eq. (3), the level set equation can be updated by the discretized Hamilton-Jacobi equation using an up-wind differential scheme in order to optimize the structural boundary.

It is noted that a level set mesh is of the same mesh size as the FE mesh corresponding to one stiffener, and that this is fixed during the optimization. It is easy therefore, to calculate the volume fraction field of the solid material on the undeformed mesh shown in Figs. 3(f)-3(h). As shown in Fig. 4(a), the structural boundary is given by the zero level set, and the LSF is used to perform the subdivision of each element into a subdomain filled with the solid material and a subdomain with the void. For the sake of simplicity, as shown in Fig. 4(b), the LSF is approximated by straight lines when searching for the intersection between the element boundary and the zero level set. Then the grey area in each element in Fig. 4(c) and the corresponding elemental volume fraction are calculated. The volume fraction fields shown in Figs. 3(f)-3(h) are thus obtained.

Based on the stiffener layout given by the LSF in Fig. 3(a), the deformed FE mesh in Fig. 3(e) can be obtained by the method presented in Section II.A. Due to the one-to-one correspondence between the elements of the level set meshes and the deformed FE mesh, a direct mapping can be used and the physical density distribution \mathbf{w} for the stiffeners is obtained by $w_j = v_j$. The density distribution is $\mathbf{w} = \mathbf{1}$ for all the elements on the skin, as shown in Fig. 3(i). Meanwhile, the geometry of the curved stiffened panels in Fig. 3 (j) can be described through the $(N + 1)$ LSFs, comprising one for the stiffener layout and N for internal topologies of N stiffeners.

It is noted that the level set method has the potential to describe arbitrary stiffener curves. However, since the free-form mesh deformation method with control mesh is utilized to adjust the FE mesh, overlap and intersection between the adjacent stiffeners are not allowed, and thus the stiffener curves are never closed in this work. The end points of the zero level set corresponding to each stiffener curve are placed on the opposite faces of the panel, but the end points of the stiffeners are free to move inside the panel due to topology optimization.

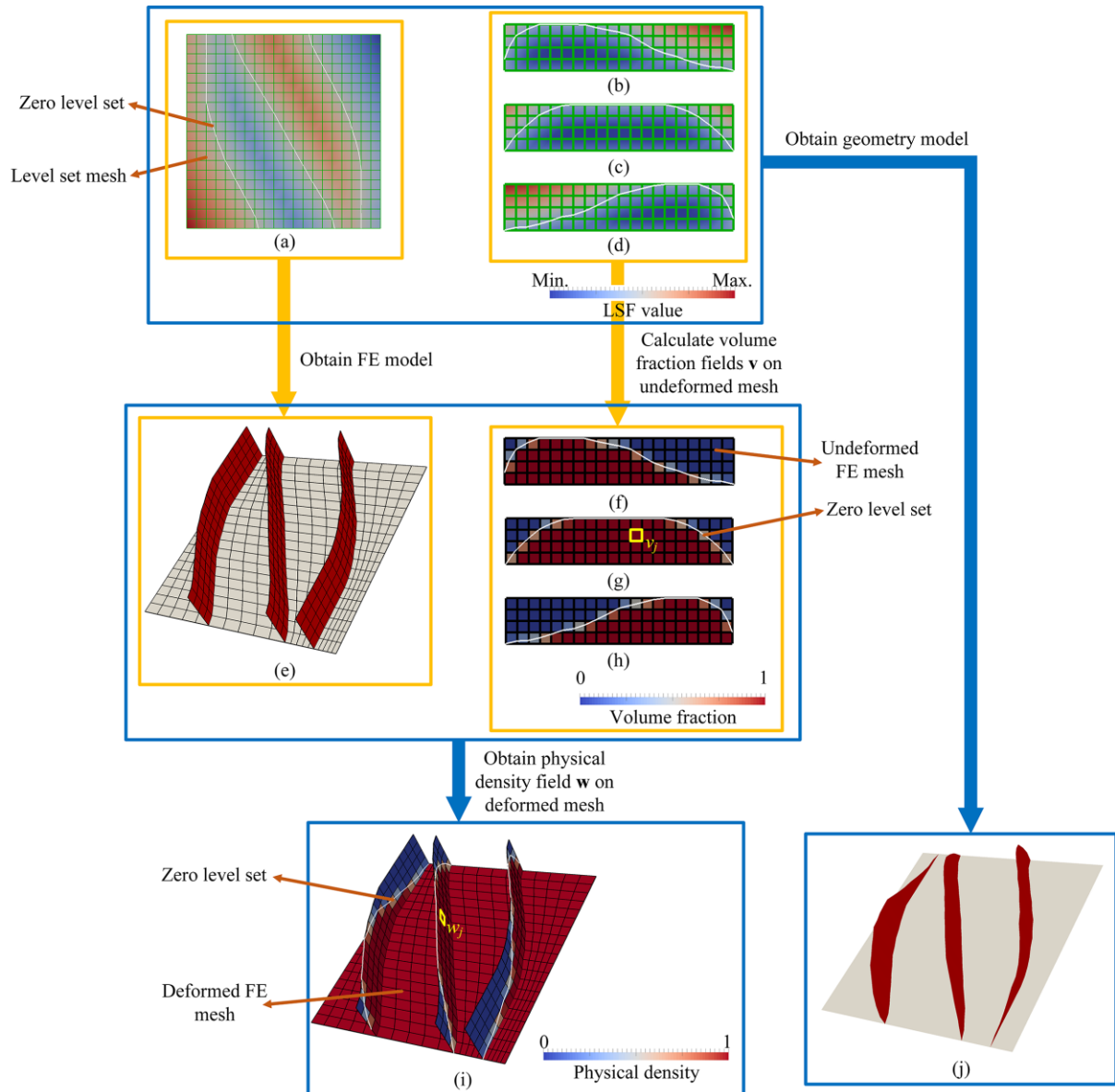


Fig. 3: Illustration of how to construct the geometry and FE models of a sample curved stiffened panel using LSFs, with white, green and black lines representing the zero level set, the level set mesh and the FE mesh respectively: (a) the LSF representing the stiffener curves, its zero level set and level set mesh; (b)-(d) the LSFs corresponding to the three stiffeners respectively, their zero level sets and level set meshes; (e) the deformed FE mesh; (f)-(h) the volume fraction fields, zero level sets and undeformed FE meshes corresponding to the three stiffeners; (i) the deformed FE mesh and corresponding physical density field; (j) the geometry model.

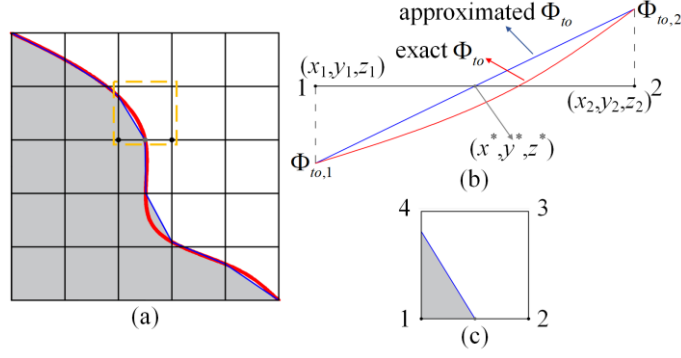


Fig. 4: Illustration of the computation of the volume fraction field on a deformed FE mesh, red and blue lines representing the zero level set and the approximated structural boundary respectively, grey region filled with the solid material: (a) the structural boundary approximated by straight lines; (b) computation of the intersection between the element boundary and the zero level set; (c) computation of the elemental volume fraction.

C. FE Analysis

After obtaining the physical density field \mathbf{w} , the stiffness and geometric stiffness matrices for the j th finite element can be calculated as [24],

$$K_j = w_j K_j^s(E_s, \rho_s, \nu, t, \mathbf{x}_{FE}) + (1 - w_j) K_j^v(E_v, \rho_v, \nu, t, \mathbf{x}_{FE}) \quad (6a)$$

$$K_{g,j} = w_j (\omega_j K_{g,j}^s(E_s, \rho_s, \nu, t, \mathbf{x}_{FE}) + (1 - w_j) K_{g,j}^v(E_v, \rho_v, \nu, t, \mathbf{x}_{FE})) \quad (6b)$$

where K_j^s and K_j^v represent the stiffness matrices of finite element j with solid and void phases, respectively. $K_{g,j}^s$ and $K_{g,j}^v$ denote the geometric stiffness matrices of finite element j with solid and void phases, respectively. E_s and ρ_s are the Young's modulus and mass density for the solid phase, while E_v and ρ_v are the Young's modulus and mass density for the void phase. ν and t are Poisson's ratio and thickness, respectively.

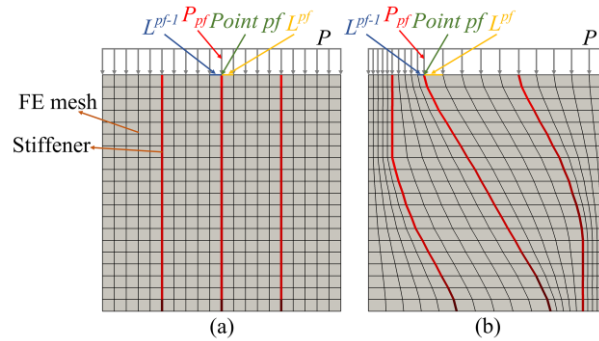


Fig.5: Illustration of the application of pressure, with black and red lines representing the FE mesh and stiffeners: (a) an example with the undeformed FE mesh; (b) an example with the deformed FE mesh.

It is noted that, when axial compression or shear loading is applied on the boundaries of curved stiffened panels with deformed FE meshes, uniform forces cannot be added directly to the corresponding nodes. As shown in Fig. 5, the force applied on the node pf is calculated as

$$P_{pf} = \frac{P(L^{pf-1} + L^{pf})}{2} \quad (7)$$

where P is the pressure value per unit length. L^{pf-1} and L^{pf} are the lengths of the elemental boundaries with the node pf , as shown in Fig. 5.

In this paper, the stationary equation (Eq. (8a)) and the linear buckling equation (Eq. (8b)) are solved using the HSL MA57 solver [37] and ARPACK [38], respectively.

$$\mathbf{K}\mathbf{u} = \mathbf{f} \quad (8a)$$

$$(\mathbf{K} + \lambda\mathbf{K}_g(\mathbf{u}))\mathbf{v} = \mathbf{0} \quad (8b)$$

where \mathbf{K} , \mathbf{u} and \mathbf{f} are the structural stiffness matrix, the stationary deflection and the applied load, respectively. \mathbf{K}_g is the structural geometric stiffness matrix. λ and \mathbf{v} represent the eigenvalue/eigenvector pair for a given buckling mode.

III. Problem Formulation and Optimization Method

In this section, the two problems considered in this work are described. To solve these two problems with a gradient-based optimizer, a semi-analytical sensitivity analysis is performed. The optimization methodology used is also presented here.

A. Problem Formulation

Both the problems of mass minimization with buckling constraint and critical buckling load factor maximization with mass constraint are investigated. As the minimum positive buckling load factor, the critical buckling load factor needs to be considered either as an objective or a constraint. The p -norm function [39] is used as a buckling aggregation function to approximate the inverse of the critical buckling load factor, that is

$$M_p = \left(\sum_{q=1}^{N_\lambda} (\mu_q)^p \right)^{1/p} \quad (9)$$

where $\mu_q = 1/\lambda_q$. λ_q is the buckling load factor for the q th mode. The first N_λ buckling modes are considered in the optimization. The approximated value M_p moves closer to the inverse of the actual minimum as the aggregation parameter p increases.

The optimization problems are formulated as follows.

- 1) Mass minimization with a buckling constraint,

$$\begin{aligned}
& \min_{\Phi_l, \Phi_{to}} m(\Phi_l, \Phi_{to}) \\
& s.t. \quad M_p(\Phi_l, \Phi_{to}) \leq 1/\lambda_{\min} \\
& \quad L_l(\Phi_l) \geq L_{\min}, \quad l = 1, 2, \dots, N_L \\
& \quad A_r(\Phi_l) \geq A_{\min}, \quad r = 1, 2, \dots, N_A \\
& \quad to = 1, 2, \dots, N
\end{aligned} \tag{10}$$

where m is the structural mass. λ_{\min} is the lower bound of the critical buckling load factor. In this work, overlap and intersection between the adjacent stiffeners are not allowed, and severely distorted elements are avoided by setting stiffener spacing and element distortion constraints to ensure the accuracy of the FEA. L denotes stiffener spacing constraints, and L_{\min} is their lower bound. A denotes element distortion constraints, and A_{\min} is their lower bound. N_L and N_A are the numbers of stiffener spacing and element distortion constraints, respectively. The mass m is defined by the mass matrix,

$$m = \mathbf{z}^T \mathbf{M} \mathbf{z} \tag{11}$$

where the vector \mathbf{z} contains one for deflection degrees of freedom along the gravity direction and zeros elsewhere.

The stiffener spacing constraints L and element distortion constraints A are evaluated using the element widths and the interior angles of the control mesh, which can be calculated through the nodal coordinates $\mathbf{x}_{\text{control}}$ of the control mesh.

- 2) Critical buckling load factor maximization with a mass constraint,

$$\begin{aligned}
& \min_{\Phi_l, \Phi_{to}} M_p(\Phi_l, \Phi_{to}) \\
& s.t. \quad m(\Phi_l, \Phi_{to}) \leq m_{\max} \\
& \quad L_l(\Phi_l) \geq L_{\min}, \quad l = 1, 2, \dots, N_L \\
& \quad A_r(\Phi_l) \geq A_{\min}, \quad r = 1, 2, \dots, N_A \\
& \quad to = 1, 2, \dots, N
\end{aligned} \tag{12}$$

where m_{\max} is the upper bound of the structural mass.

B. Sensitivity analysis

In order to solve Eqs. (10) and (12) using a gradient-based optimizer, the sensitivities of the p -norm function M_p , the mass m , the stiffener spacing L and the element distortion A are needed. To obtain these sensitivities, semi-analytical method is used. First, the derivative of λ_q with respect to changes in the nodal coordinates of the control mesh y_i is computed using the adjoint method [40]. Eq. (8b) and Eq. (8a) are pre-multiplied by the eigenvector \mathbf{v}_q and the adjoint vector \mathbf{u}_{ad} ,

$$\mathbf{v}_q^T (\mathbf{K} + \lambda_q \mathbf{K}_g(\mathbf{u})) \mathbf{v}_q = 0 \quad (13a)$$

$$\mathbf{u}_{ad}^T (\mathbf{K}\mathbf{u} - \mathbf{f}) = 0 \quad (13b)$$

Then adding them and differentiating,

$$\mathbf{v}_q^T (\mathbf{K} + \lambda_q \mathbf{K}_g(\mathbf{u})) \mathbf{v}_q - \mathbf{u}_{ad}^T (\mathbf{K}\mathbf{u} - \mathbf{f}) = 0 \quad (14a)$$

$$\begin{aligned} & 2\mathbf{v}_q^T (\mathbf{K} + \lambda_q \mathbf{K}_g(\mathbf{u})) \frac{\partial \mathbf{v}_q}{\partial y_i} \\ & + \mathbf{v}_q^T \left(\frac{\partial \mathbf{K}}{\partial y_i} + \frac{\partial \lambda_q}{\partial y_i} \mathbf{K}_g(\mathbf{u}) + \lambda_q \frac{\partial \mathbf{K}_g(\mathbf{u})}{\partial y_i} + \lambda_q \frac{\partial \mathbf{K}_g(\mathbf{u})}{\partial u} \frac{\partial u}{\partial y_i} \right) \mathbf{v}_q \\ & - \frac{\partial \mathbf{u}_{ad}^T}{\partial y_i} (\mathbf{K}\mathbf{u} - \mathbf{f}) - \mathbf{u}_{ad}^T \left(\frac{\partial \mathbf{K}}{\partial y_i} \mathbf{u} + \mathbf{K} \frac{\partial \mathbf{u}}{\partial y_i} - \frac{d\mathbf{f}}{dy_i} \right) = 0 \end{aligned} \quad (14b)$$

By collecting the terms involving $\partial \mathbf{u}/\partial y_i$ in Eq. (14b) and setting them to zero, the derivative of λ_q with respect to y_i can be calculated by,

$$\frac{\partial \lambda_q}{\partial y_i} = \frac{\mathbf{u}_{ad}^T \left(\frac{\partial \mathbf{K}}{\partial y_i} \mathbf{u} - \frac{d\mathbf{f}}{dy_i} \right) - \mathbf{v}_q^T \left(\frac{\partial \mathbf{K}}{\partial y_i} + \lambda_q \frac{\partial \mathbf{K}_g(\mathbf{u})}{\partial y_i} \right) \mathbf{v}_q}{\mathbf{v}_q^T \mathbf{K}_g(\mathbf{u}) \mathbf{v}_q} \quad (15)$$

where

$$\lambda_q \mathbf{v}_q^T \frac{\partial \mathbf{K}_g(\mathbf{u})}{\partial u} \mathbf{v}_q = \mathbf{u}_{ad}^T \mathbf{K} \quad (16)$$

In a similar way, the derivative of λ_q with respect to the physical density w_j can be obtained by,

$$\frac{\partial \lambda_q}{\partial w_j} = \frac{\mathbf{u}_{ad}^T \left(\frac{\partial \mathbf{K}}{\partial w_j} \mathbf{u} - \frac{\partial \mathbf{f}}{\partial w_j} \right) - \mathbf{v}_q^T \left(\frac{\partial \mathbf{K}}{\partial w_j} + \lambda_q \frac{\partial \mathbf{K}_g(\mathbf{u})}{\partial w_j} \right) \mathbf{v}_q}{\mathbf{v}_q^T \mathbf{K}_g(\mathbf{u}) \mathbf{v}_q} \quad (17)$$

where

$$\lambda_q \mathbf{v}_q^T \frac{\partial \mathbf{K}_g(\mathbf{u})}{\partial u} \mathbf{v}_q = \mathbf{u}_{ad}^T \mathbf{K} \quad (18)$$

It is noted that $\partial \mathbf{f} / \partial y_i \neq \mathbf{0}$ in Eq. (15) because the update of \mathbf{y} leads to the re-distribution of the force applied to the nodes of the FE mesh via Eq. (7). Since self-weight is ignored in this work, $\partial \mathbf{f} / \partial w_j = 0$, and Eq. (17) can be simplified to,

$$\frac{\partial \lambda_q}{\partial w_j} = \frac{\mathbf{u}_{ad}^T \frac{\partial \mathbf{K}}{\partial w_j} \mathbf{u} - \mathbf{v}_q^T \left(\frac{\partial \mathbf{K}}{\partial w_j} + \lambda_q \frac{\partial \mathbf{K}_g(\mathbf{u})}{\partial w_j} \right) \mathbf{v}_q}{\mathbf{v}_q^T \mathbf{K}_g(\mathbf{u}) \mathbf{v}_q} \quad (19)$$

It is noted that when multiple eigenvalues exist, the individual eigenvalues may not be differentiable. However, since multiple eigenvalues are not found in the numerical examples in Section 4, this issue is not discussed in this paper.

From Eq. (9), the derivatives of M_p with respect to y_i and w_j can be obtained as,

$$\frac{\partial M_p}{\partial y_i} = M_p^{1-p} \sum_{q=1}^{N_i} \left(\mu_q^{p-1} (-\lambda_q^{-2}) \frac{\partial \lambda_q}{\partial y_i} \right) \quad (20a)$$

$$\frac{\partial M_p}{\partial w_j} = M_p^{1-p} \sum_{q=1}^{N_i} \left(\mu_q^{p-1} (-\lambda_q^{-2}) \frac{\partial \lambda_q}{\partial w_j} \right) \quad (20b)$$

Based on Eq. (11), the derivatives of m with respect to y_i and w_j can be calculated by,

$$\frac{\partial m}{\partial y_i} = \mathbf{z}^T \frac{\partial \mathbf{M}}{\partial y_i} \mathbf{z} \quad (21a)$$

$$\frac{\partial m}{\partial w_j} = \mathbf{z}_i^T \frac{\partial \mathbf{M}_i}{\partial w_j} \mathbf{z}_i \quad (21b)$$

$\partial \mathbf{f} / \partial y_i$, $\partial \mathbf{K} / \partial y_i$, $\partial \mathbf{K}_g / \partial y_i$ and $\partial \mathbf{M} / \partial y_i$ in Eqs. (15) and (21a), as well as the derivatives dL_i / dy_i and dA_i / dy_i related to the spacing and element distortion constraints, can then be approximated via the central finite difference method, since

it is easy to implement. Because y_i is the change in the nodal coordinates of the control mesh and is used to calculate the nodal coordinates of the finite elements via Eq. (4), finite differences are only performed on the element level. Additional FEAs are not needed. This ensures the efficiency of the evaluation. When using the central finite difference method, it is suggested that the smallest possible perturbations are chosen to ensure that the accuracy of the calculation can be guaranteed. In this work, the perturbation is chosen as $0.0001a_0$, where a_0 is the initial FE element width. The calculated sensitivities $\partial g/\partial y_i$ in Eqs. (20a) and (21a) have been compared with $(g(y_{i,0} + \Delta y_i) - g(y_{i,0} - \Delta y_i))/2\Delta y_i$, where g represents an arbitrary equation, i.e. M_p and m . The error in mass sensitivity is within 0.1%, and the errors in buckling sensitivities are within 1% when there is no mode switching, which shows the accuracy of the sensitivity calculation.

It is noted that, in optimization, the LSFs are always maintained as signed distance functions to ensure a well-behaved boundary. In order to convert an arbitrary LSF to a signed distance function with the same boundary locations, a combination of the marching squares and fast marching algorithms [31] is applied. In order to ensure the signed distance property $|\nabla\Phi|=1$ after every update of the LSF, the fast velocity extension algorithm [41] is utilized. In Eq. (2), the relationship between the changes of the LSF values $\Delta\Phi_b$ at the boundary and $\Delta\Phi$ in the rest of the design domain is determined, as

$$\Delta\Phi = \left[\frac{\partial\Phi}{\partial\Phi_b} \right] \Delta\Phi_b \quad (22)$$

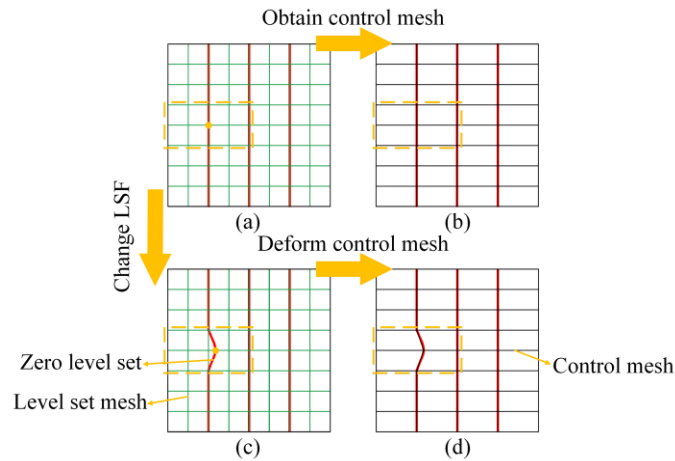


Fig.6: Illustration of how to compute the term of $\partial y_i/\partial \Phi_{l,b}$, with red, green and black lines representing the zero level set, the level set mesh and the control mesh respectively: (a) the zero level set before perturbation and the level set mesh; (b) the zero level set and the corresponding control mesh before perturbation; (c) the

zero level set after perturbation; (d) the control mesh, deformed in accordance with the change of the zero level set after perturbation.

To update the LSF representing the stiffener layout, the derivatives with respect to y_i are further mapped to the level set value of the boundary points $\Phi_{l,b}$ through the chain rule,

$$\frac{\partial g}{\partial \Phi_{l,b}} = \sum_i \frac{\partial g}{\partial y_i} \frac{\partial y_i}{\partial \Phi_{l,b}} \quad (23)$$

where g is the general function representing the p -norm function M_p , the mass m , the stiffener spacing L and the element distortion A . The term $\partial y_i / \partial \Phi_{l,b}$ is computed by perturbing the level set boundary implicitly, as shown in Fig. 6. For a given boundary point of interest, a small perturbation $\Delta \Phi_{l,b}$ is assigned to its level set value $\Phi_{l,b}$. The change in the LSF $\Delta \Phi_l$ can be obtained via Eq. (22). After implementing the marching squares and fast marching algorithms, as shown in Fig. 6(c), the new LSF and the corresponding zero level set are achieved. This results in a new y_i . The control mesh is deformed, which is shown in Fig. 6(d). Then using the central finite difference method, the term $\partial y_i / \partial \Phi_{l,b}$ can be approximated by,

$$\frac{\partial y_i}{\partial \Phi_{l,b}} = \frac{y_i|_{\Phi_{l,b}=\Phi_{l,b}+\Delta\Phi_{l,b}} - y_i|_{\Phi_{l,b}=\Phi_{l,b}-\Delta\Phi_{l,b}}}{2\Delta\Phi_{l,b}} \quad (24)$$

where the perturbation $\Delta \Phi_{l,b}$ is chosen as $0.001b_{l,0}$, where $b_{l,0}$ is the element width of the level set mesh used to describe the stiffener layout.

To update the LSFs representing the stiffener internal topologies, the derivatives with respect to w_j are further mapped to the level set values of the boundary points $\Phi_{to,b}$ through the chain rule,

$$\frac{\partial g}{\partial \Phi_{to,b}} = \sum_j \frac{\partial g}{\partial w_j} \frac{\partial w_j}{\partial v_j} \frac{\partial v_j}{\partial \Phi_{to,b}} \quad (25)$$

where $\partial w_j / \partial v_j = 1$ because $w_j = v_j$. In the same way as for the term $\partial y_i / \partial \Phi_{l,b}$, the term of $\partial v_j / \partial \Phi_{to,b}$ is computed via the implicit perturbation of the level set boundary, which is shown in Fig. 7. A small perturbation $\Delta \Phi_{to,b}$ is assigned to the level set value $\Phi_{to,b}$ of the given boundary point of interest. The change in the LSF $\Delta \Phi_{to}$ can be obtained via Eq. (22). After implementing the marching squares and fast marching algorithms, as shown in Fig. 7(b), the new LSF and

corresponding zero level set are achieved. This results in the new volume fraction v_j . Then using the central finite difference method, the term $\partial v_j / \partial \Phi_{to,b}$ can be approximated by,

$$\frac{\partial v_j}{\partial \Phi_{to,b}} = \frac{v_j|_{\Phi_{to,b}=\Phi_{to,b}+\Delta\Phi_{to,b}} - v_j|_{\Phi_{to,b}=\Phi_{to,b}-\Delta\Phi_{to,b}}}{2\Delta\Phi_{to,b}} \quad (26)$$

where the perturbation $\Delta\Phi_{to,b}$ is chosen as $0.001b_{to,0}$, where $b_{to,0}$ is the element width of the level set mesh used to describe the stiffer internal topology.

Using the gradient-based optimization method with the sensitivity information in Eqs. (23) and (25), $\Delta\Phi_{l,b}$ and $\Delta\Phi_{to,b}$ can be obtained. Following this $\Delta\Phi_l$ and $\Delta\Phi_{to}$ can be calculated via Eq. (22) such that $|\nabla(\Phi+\Delta\Phi)|=1$. It is noted that, since the fast velocity extension algorithm is only first order accurate, the LSFs are re-initialized using the fast marching method after each update in this work.

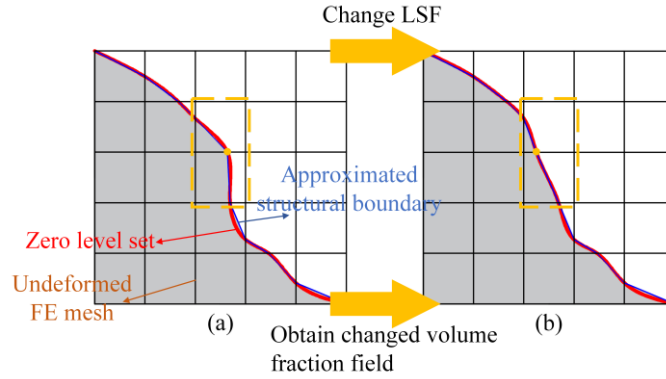


Fig.7: Illustration of the computation of the term $\partial v_i / \partial \Phi_{to,b}$, with red, blue and black lines representing the zero level set, the approximated structural boundary and the undeformed FE mesh respectively: the structural boundary and material distribution (a) before perturbation; (b) after perturbation.

C. Optimization Algorithm

The IPOPT algorithm [32] is used to solve the optimization problems described in Eqs. (10) and (12) at each iteration to obtain $\Delta\Phi_{l,b}$ and $\Delta\Phi_{to,b}$ in order to update the curved stiffened panels. Linearization of the optimization problems using Taylor's expansion can then be performed as follows.

- 1) Mass minimization with a buckling constraint,

$$\begin{aligned}
& \min_{\Delta\Phi_{l,b}, \Delta\Phi_{to,b}} m_0 + \left[\frac{\partial m}{\partial \Phi_{l,b}} \right]^T \Delta\Phi_{l,b} + \sum_{to=1}^N \left[\frac{\partial m}{\partial \Phi_{to,b}} \right]^T \Delta\Phi_{to,b} \\
& \text{s.t. } M_{p,0} + \left[\frac{\partial M_p}{\partial \Phi_{l,b}} \right]^T \Delta\Phi_{l,b} + \sum_{to=1}^N \left[\frac{\partial M_p}{\partial \Phi_{to,b}} \right]^T \Delta\Phi_{to,b} \leq \frac{1}{\lambda_{\min}} \\
& L_{l,0} + \left[\frac{dL_l}{d\Phi_{l,b}} \right]^T \Delta\Phi_{l,b} \geq L_{\min}, \quad l = 1, 2, \dots, N_L \\
& A_{r,0} + \left[\frac{dA_r}{d\Phi_{l,b}} \right]^T \Delta\Phi_{l,b} \geq L_{\min}, \quad r = 1, 2, \dots, N_A \\
& -\gamma_1 \leq \Delta\Phi_{l,b} \leq \gamma_1 \\
& -\gamma_2 \leq \Delta\Phi_{to,b} \leq \gamma_2 \\
& to = 1, 2, \dots, N
\end{aligned} \tag{27}$$

2) Critical buckling load factor maximization with a mass constraint,

$$\begin{aligned}
& \min_{\Delta\Phi_{l,b}, \Delta\Phi_{to,b}} M_{p,0} + \left[\frac{\partial M_p}{\partial \Phi_{l,b}} \right]^T \Delta\Phi_{l,b} + \sum_{to=1}^N \left[\frac{\partial M_p}{\partial \Phi_{to,b}} \right]^T \Delta\Phi_{to,b} \\
& \text{s.t. } m_0 + \left[\frac{\partial m}{\partial \Phi_{l,b}} \right]^T \Delta\Phi_{l,b} + \sum_{to=1}^N \left[\frac{\partial m}{\partial \Phi_{to,b}} \right]^T \Delta\Phi_{to,b} \leq m_{\max} \\
& L_{l,0} + \left[\frac{dL_l}{d\Phi_{l,b}} \right]^T \Delta\Phi_{l,b} \geq L_{\min}, \quad l = 1, 2, \dots, N_L \\
& A_{r,0} + \left[\frac{dA_r}{d\Phi_{l,b}} \right]^T \Delta\Phi_{l,b} \geq L_{\min}, \quad r = 1, 2, \dots, N_A \\
& -\gamma_1 \leq \Delta\Phi_{l,b} \leq \gamma_1 \\
& -\gamma_2 \leq \Delta\Phi_{to,b} \leq \gamma_2 \\
& to = 1, 2, \dots, N
\end{aligned} \tag{28}$$

where $M_{p,0}$, m_0 , $L_{l,0}$ and $A_{r,0}$ are the values at the current iteration. γ_1 and γ_2 are the move limits for $\Delta\Phi_{l,b}$ and $\Delta\Phi_{to,b}$, respectively.

The proposed method is illustrated in Fig. 8.

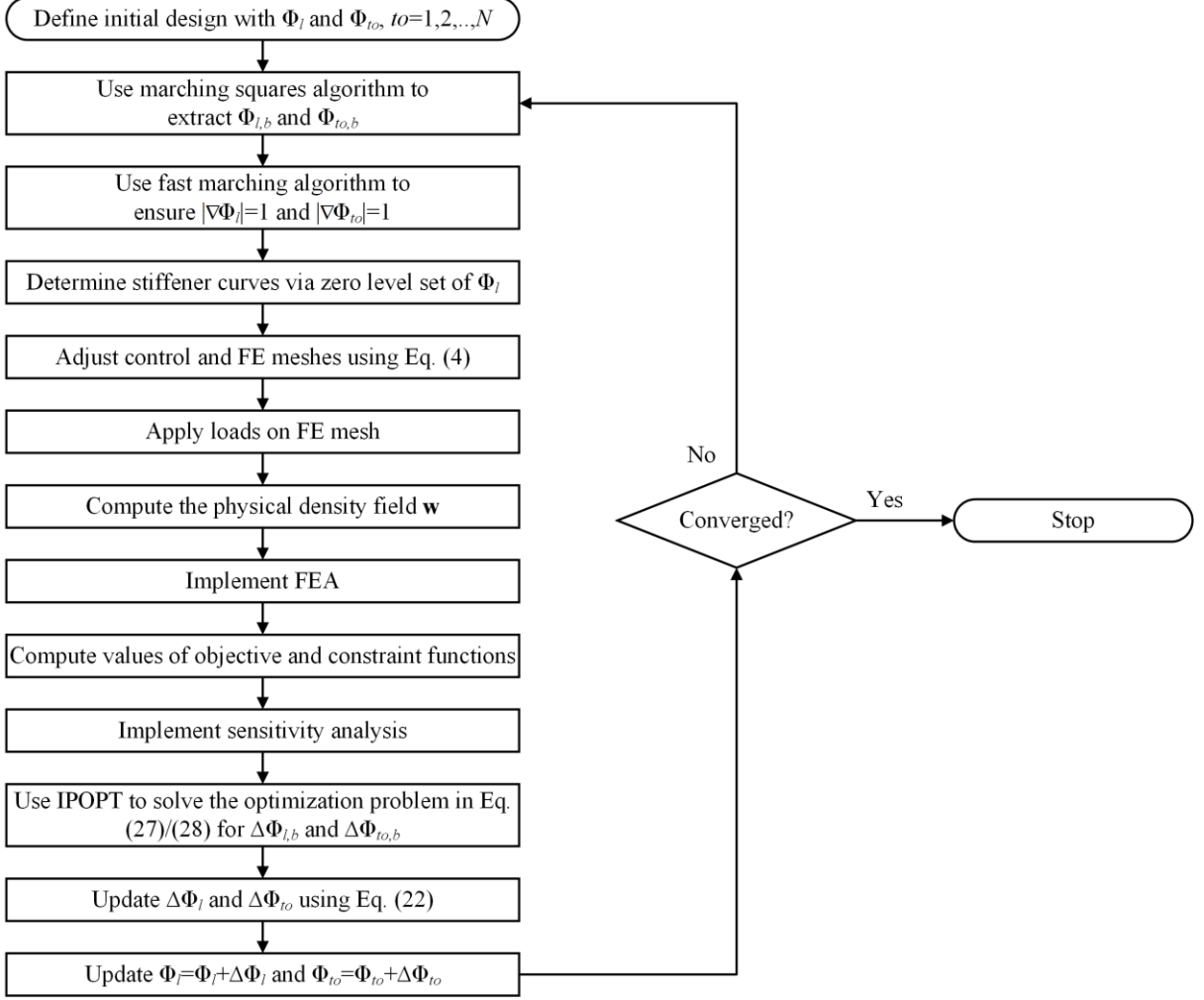


Fig. 8: Flowchart of the proposed method.

IV. Numerical examples

Two numerical examples are presented to demonstrate the application of the proposed method for the simultaneous layout and topology optimization of curved stiffened panels. The Young's modulus of the solid material is $E_s = 73$ GPa and the Young's modulus of the void phase is $E_v = 10^{-6} \times 73$ GPa. The density is $\rho_s = 2795$ kg/m³ for the solid material and $\rho_v = 0$ for the void phase. The Poisson's ratio is $\nu = 0.33$. The thicknesses of both the skin and the stiffeners is $t = 0.002$ m.

A. Example 1: mass minimization with buckling constraint

For buckling-constrained problems, the p -norm function M_p cannot be applied directly to enforce a constraint on the inverse of the minimum positive buckling load factor. This is because, in Eq. (9), a finite p needs to be chosen for

numerical stability, which leads to the p -norm function value being greater than the inverse of the minimum. An adaptive scaling constraint [39, 42] similar to that for stress-constrained problems is adopted to make the p -norm function value closer to the inverse of the critical buckling load factor,

$$\alpha_1 M_p \leq \frac{1}{\lambda_{\min}} \quad (29)$$

where $\alpha_1^k = \frac{1}{\lambda_1^k M_p^k}$ at the k th iteration.

When IPOPT is used to solve the problem described by Eq. (29), the buckling constraint is approximated as,

$$\alpha_1 [M_p^k]_{\text{approximation}} = \alpha_1 \left(M_p^{k-1} + \left[\frac{\partial M_p}{\partial \Phi_{l,b}} \right]_{k-1}^T \Delta \Phi_{l,b,k-1} + \sum_{to=1}^N \left[\frac{\partial M_p}{\partial \Phi_{to,b}} \right]_{k-1}^T \Delta \Phi_{to,b,k-1} \right) \leq \frac{1}{\lambda_{\min}} \quad (30)$$

Using IPOPT, only the constraint in Eq. (30) is satisfied at each iteration of the optimization. However, since only first-order sensitivity information is used and higher-order sensitivity information is ignored, the prediction of the p -norm function $[M_p^k]_{\text{approximation}}$ from Eq. (30) is not sufficiently accurate and may be slightly smaller than the real one M_p^k . This may lead to the violation of the actual buckling constraint $\lambda_1 \geq \lambda_{\min}$. Therefore, an additional adaptive scaling constraint scheme is introduced and Eq. (29) is re-written as

$$\alpha_1 \alpha_2 M_p \leq \frac{1}{\lambda_{\min}} \quad (31)$$

where $\alpha_2^k = \frac{M_p^k}{[M_p^k]_{\text{approximation}}}$.

The mass minimization problem with buckling constraint at each iteration in Eq. (27) can therefore be re-written as

$$\begin{aligned}
& \min_{\Delta\Phi_{l,b}, \Delta\Phi_{to,b}} m_0 + \left[\frac{\partial m}{\partial \Phi_{l,b}} \right]^T \Delta\Phi_{l,b} + \sum_{to=1}^N \left[\frac{\partial m}{\partial \Phi_{to,b}} \right]^T \Delta\Phi_{to,b} \\
& s.t. \quad M_{p,0} + \left[\frac{\partial M_p}{\partial \Phi_{l,b}} \right]^T \Delta\Phi_{l,b} + \sum_{to=1}^N \left[\frac{\partial M_p}{\partial \Phi_{to,b}} \right]^T \Delta\Phi_{to,b} \leq \frac{1}{\alpha_1 \alpha_2 \lambda_{\min}} \\
& \quad L_{l,0} + \left[\frac{dL_l}{d\Phi_{l,b}} \right]^T \Delta\Phi_{l,b} \geq L_{\min}, \quad l = 1, 2, \dots, N_L \\
& \quad A_{r,0} + \left[\frac{dA_r}{d\Phi_{l,b}} \right]^T \Delta\Phi_{l,b} \geq L_{\min}, \quad r = 1, 2, \dots, N_A \\
& \quad -\gamma_1 \leq \Delta\Phi_{l,b} \leq \gamma_1 \\
& \quad -\gamma_2 \leq \Delta\Phi_{to,b} \leq \gamma_2 \\
& \quad to = 1, 2, \dots, N
\end{aligned} \tag{32}$$

A stiffened panel with the loading and boundary conditions shown in Fig. 9 is considered for optimization. The bottom edge of the panel is fixed, and a shear load $P = 300$ kN/m is applied on the top edge. The initial design, which comprises a $0.3 \text{ m} \times 0.3 \text{ m}$ skin and 7 vertical stiffeners, each with a depth of 0.03 m is given in Fig. 10. The FE mesh comprises 80×80 plate elements for the skin, with 8 elements through the depth of each of the stiffeners. Eight LSFs are used, comprising one representing the stiffener curves and seven for the internal topologies of the stiffeners. The first 50 buckling modes are considered in the optimization. For the p -norm function, the aggregation parameter $p = 12$ is used. The lower bound of the critical buckling load factor $\lambda_{\min} = 1$.

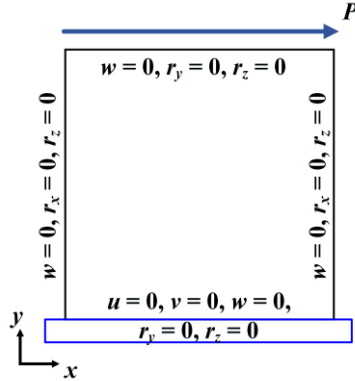


Fig. 9: Loading and boundary conditions for the design of a stiffened panel under shear loading.

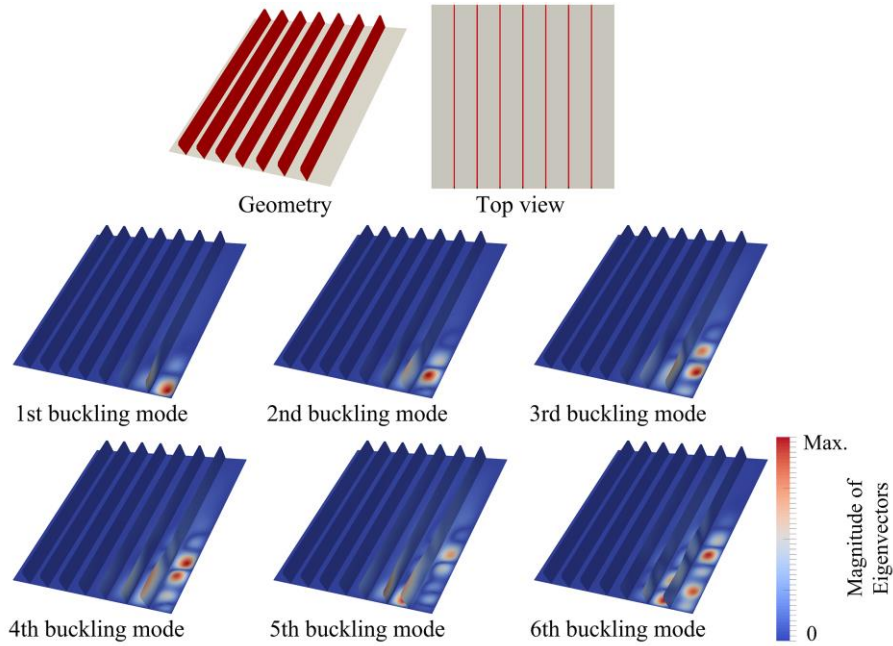


Fig. 10: Initial design with 7 vertical stiffeners, $m = 0.855$ kg, and its first 6 buckling modes under shear loading, $\lambda_1 = 1.141$, $\lambda_2 = 1.459$, $\lambda_3 = 1.702$, $\lambda_4 = 1.903$, $\lambda_5 = 2.089$, $\lambda_6 = 2.155$.

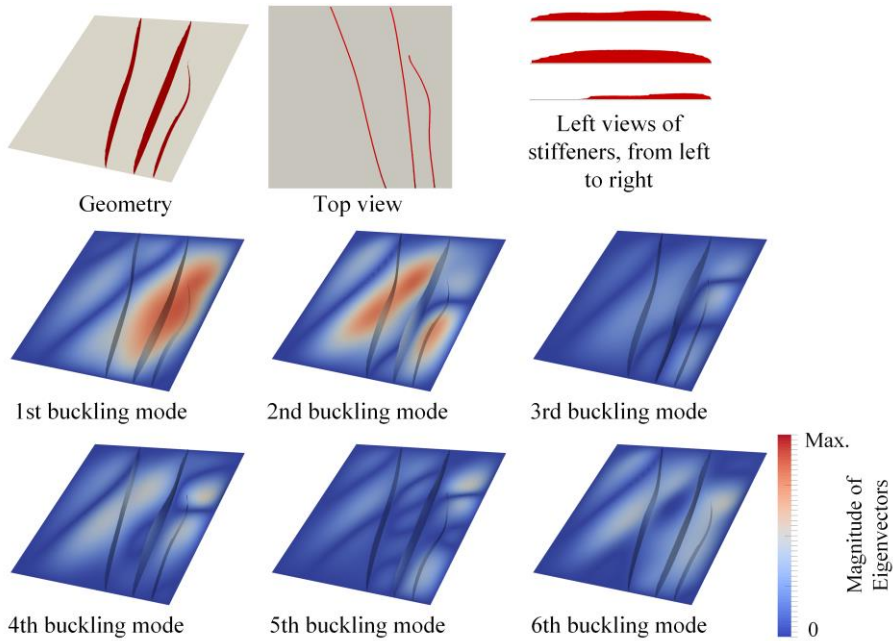


Fig. 11: Optimized design considering initial design with 7 vertical stiffeners, $m = 0.563$ kg, and its first 6 buckling modes under shear loading, $\lambda_1 = 1.008$, $\lambda_2 = 1.077$, $\lambda_3 = 1.102$, $\lambda_4 = 1.122$, $\lambda_5 = 1.246$, $\lambda_6 = 1.256$.

The optimized design is shown in Fig. 11. Compared with the initial design, the mass is decreased by 34.1%. Despite this, the critical buckling load factor $\lambda_1 = 1.008$ and the buckling constraint is satisfied. It can be observed

that, by using topology optimization, the number of stiffeners and the internal topology, height and width of each of them are optimized. From the initial design and corresponding buckling modes in Fig. 10, it can be seen that buckling tends to occur towards the right side of the panel under the given load case since this is the area where the greatest compression due to in-plane bending occurs. In order to increase the stiffness in these regions, the three stiffeners which remain are moved to the right hand side of structure. It can also be seen that for each stiffener in the optimized design, the depth of the central part of the stiffeners is greater than that at the ends, to increase out-of-plane stiffness in this unsupported region (ends are prevented from deflecting out of plane) and defer overall buckling modes.

We also perform an optimization where the layout design variables are excluded. The same initial design with 7 vertical stiffeners shown in Fig. 10 is used. The result is presented in Fig. 12. Here, the layout of the stiffeners is frozen, with only the number and topologies of the stiffeners optimized. The mass of the optimized design in Fig. 11 with simultaneous layout and topology optimization is 0.563 kg, while the optimized design in Fig. 12 without the layout design variables is 0.594 kg, a 5.4% difference. In comparison with the optimized design in Fig. 11, more stiffeners with greater depth are required in the optimized design in Fig. 12. In terms of the mass of the stiffeners, there is a 50.9% difference between the two optimized designs. This shows the simultaneous layout and topology optimization allows a further significant reduction in the panel's weight.

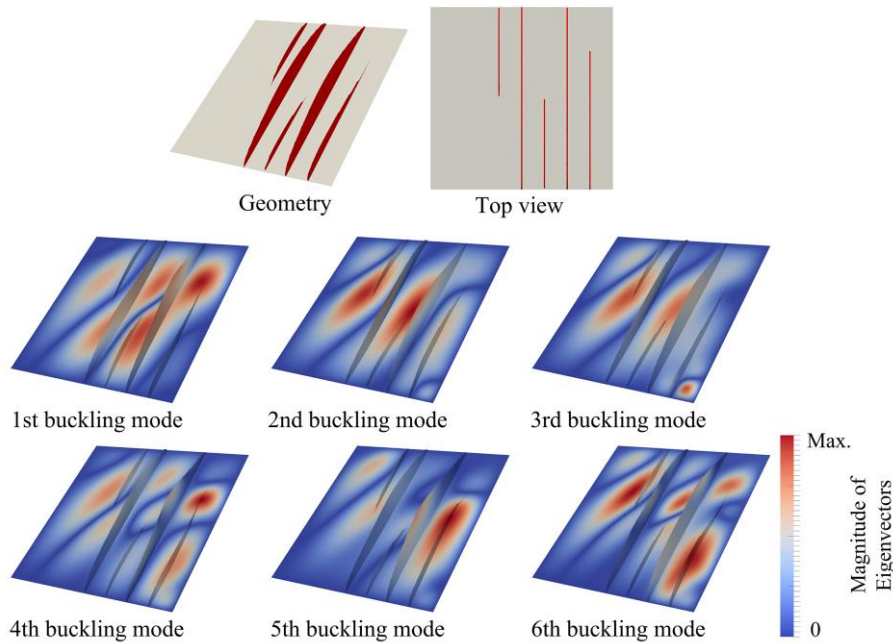


Fig. 12: Optimized design without the layout optimization, considering initial design with 7 vertical stiffeners, $m = 0.594$ kg, and its first 6 buckling modes under shear loading, $\lambda_1 = 1.000$, $\lambda_2 = 1.039$, $\lambda_3 = 1.064$, $\lambda_4 = 1.170$, $\lambda_5 = 1.182$, $\lambda_6 = 1.293$.

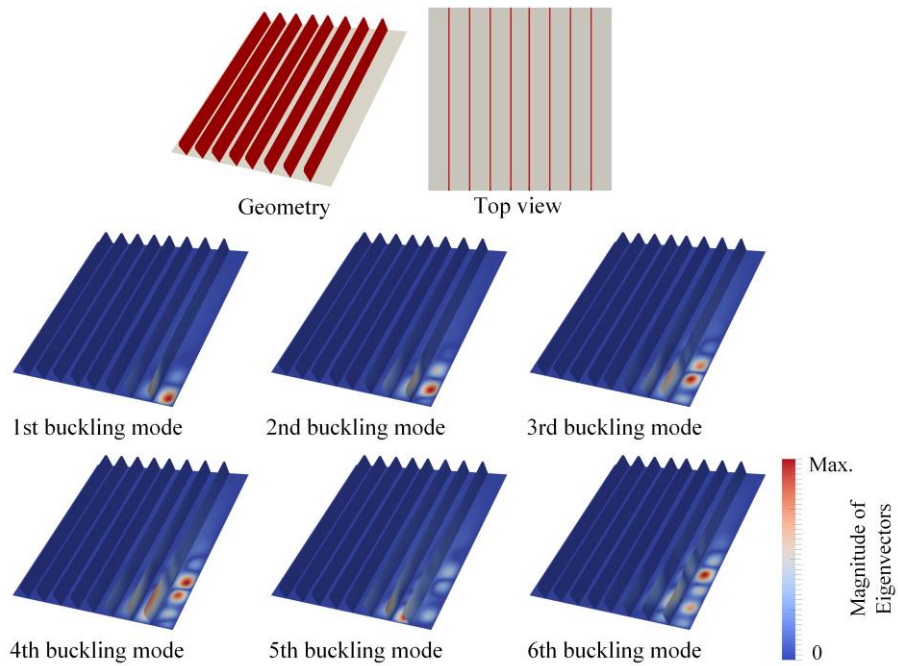


Fig. 13: Initial design with 8 vertical stiffeners, $m = 0.905$ kg, and its first 6 buckling modes under shear loading, $\lambda_1 = 1.364$, $\lambda_2 = 1.744$, $\lambda_3 = 2.027$, $\lambda_4 = 2.255$, $\lambda_5 = 2.412$, $\lambda_6 = 2.522$.

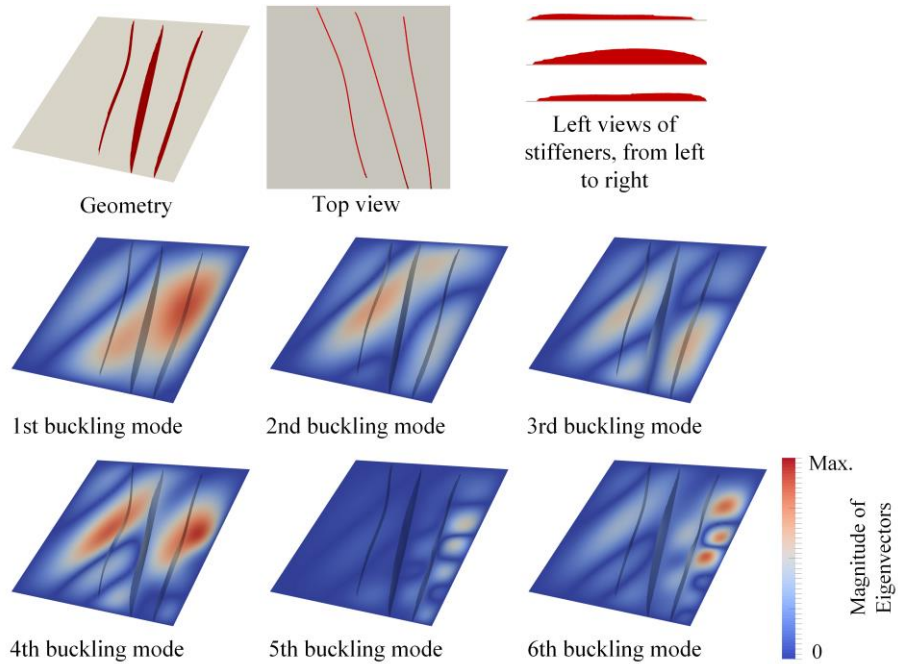


Fig. 14: Optimized design considering initial design with 8 vertical stiffeners, $m = 0.564$ kg, and its first 6 buckling modes under shear loading, $\lambda_1 = 1.002$, $\lambda_2 = 1.061$, $\lambda_3 = 1.119$, $\lambda_4 = 1.190$, $\lambda_5 = 1.248$, $\lambda_6 = 1.253$.

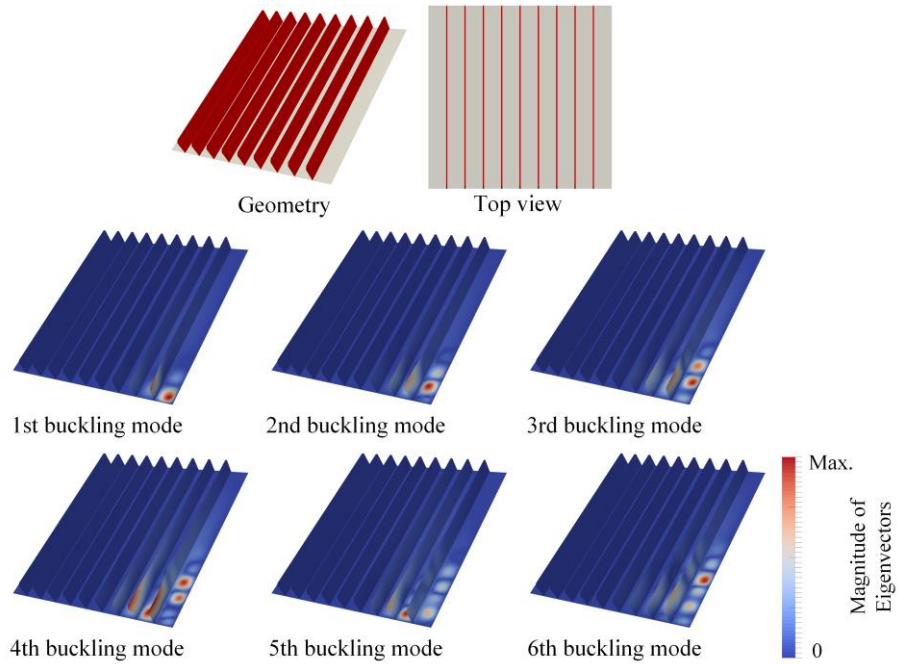


Fig. 15: Initial design with 9 vertical stiffeners, $m = 0.955$ kg, and its first 6 buckling modes under shear loading, $\lambda_1 = 1.667$, $\lambda_2 = 2.134$, $\lambda_3 = 2.475$, $\lambda_4 = 2.731$, $\lambda_5 = 2.837$, $\lambda_6 = 3.046$.

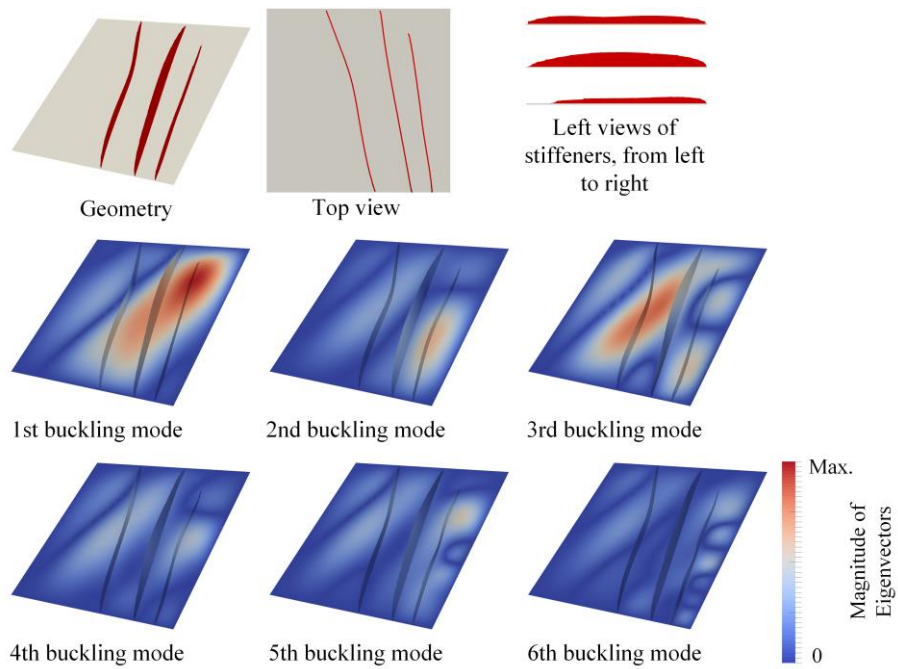


Fig. 16: Optimized design considering initial design with 9 vertical stiffeners, $m = 0.565$ kg, and its first 6 buckling modes under shear loading, $\lambda_1 = 1.008$, $\lambda_2 = 1.058$, $\lambda_3 = 1.108$, $\lambda_4 = 1.196$, $\lambda_5 = 1.298$, $\lambda_6 = 1.316$.

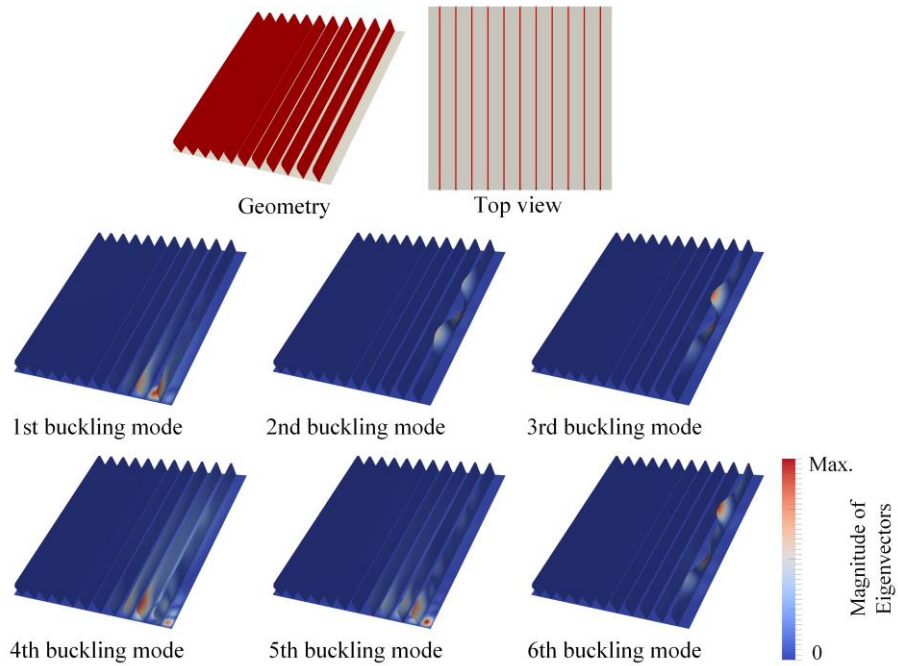


Fig. 17: Initial design with 11 vertical stiffeners, $m = 1.056$ kg, and its first 6 buckling modes under shear loading, $\lambda_1 = 3.153$, $\lambda_2 = 3.2322$, $\lambda_3 = 3.2325$, $\lambda_4 = 3.848$, $\lambda_5 = 3.992$, $\lambda_6 = 4.193$.

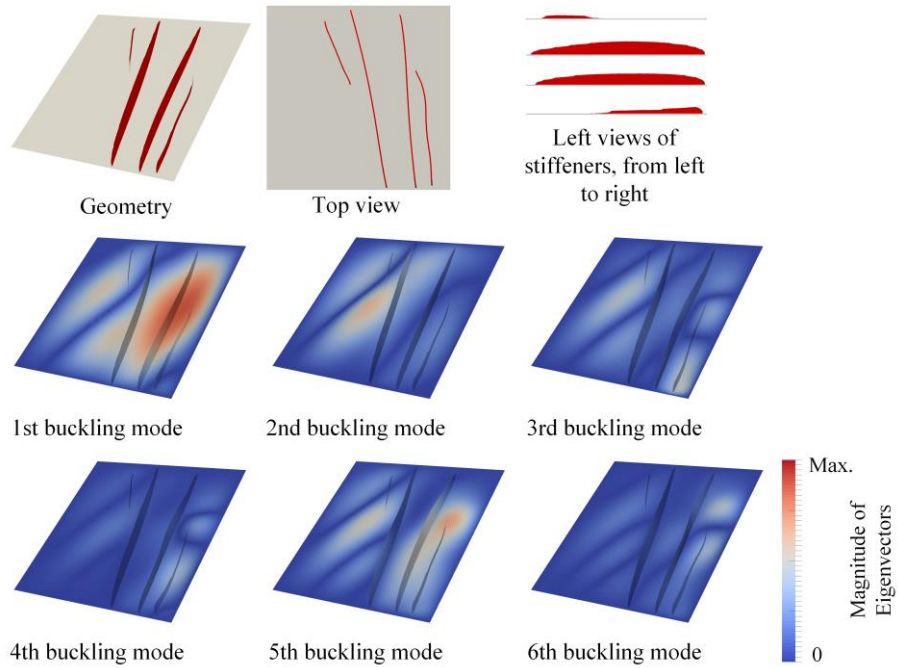


Fig. 18: Optimized design at 1500th iteration, considering initial design with 11 vertical stiffeners, $m = 0.562$ kg, and its first 6 buckling modes under shear loading, $\lambda_1 = 1.006$, $\lambda_2 = 1.047$, $\lambda_3 = 1.099$, $\lambda_4 = 1.145$, $\lambda_5 = 1.163$, $\lambda_6 = 1.216$.

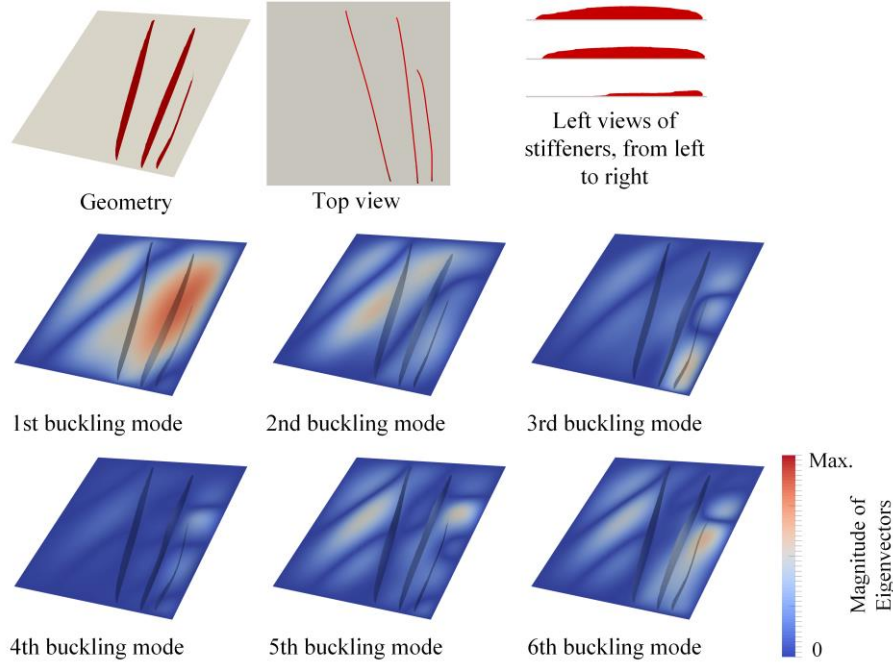


Fig. 19: Optimized design at 2500th iteration, considering initial design with 11 vertical stiffeners, $m = 0.559$ kg, and its first 6 buckling modes under shear loading, $\lambda_1 = 1.003$, $\lambda_2 = 1.085$, $\lambda_3 = 1.142$, $\lambda_4 = 1.163$, $\lambda_5 = 1.220$, $\lambda_6 = 1.254$.

To investigate the influence of the initial configurations, the optimization problem is also solved considering initial designs with different numbers of stiffeners. The maximum number of iterations is 1500. The initial designs are shown in Figs. 13, 15 and 17. The corresponding results are given in Figs. 14, 16 and 18, respectively. The differences between their masses are within 0.54%. It can be observed that, three stiffeners remain in the optimized designs in Figs. 14 and 16, while there are four stiffeners left in the optimized designs in Fig. 18. When we extend the maximum number of iterations to 2500 for the optimization considering the initial design with 11 vertical stiffeners, it is found in Fig. 19 that the extra stiffener is removed. However, the mass is only reduced by 0.53%, compared to that of the optimized design using 1500 iterations. Considering the computational cost, it may not be worth continuing to optimize the structure after 1500 iterations. It can be also observed that all the optimized designs follow the same trends. The remaining stiffeners are moved to the right hand side of the panel to increase the stiffness in the bottom right hand region of the panel. Therefore, even though initial designs with different numbers of stiffeners are selected, the proposed method has the potential to find promising results within the corresponding limited design space.

B. Example 2: critical buckling load factor maximization with mass constraint

A stiffened panel with the same loading and boundary conditions as in Fig. 9 is considered for optimization of critical buckling load with mass constraint. The same initial design with 7 vertical stiffeners shown in Fig. 10 is used. All the FEA and optimization parameters are the same as those in Example 1. The upper bound of the stiffener mass is set to 17% of the initial design, i.e., the upper bound of the structural mass $m_{max} = 0.563$ kg which is that of the optimized design obtained from the mass minimization with a buckling constraint.

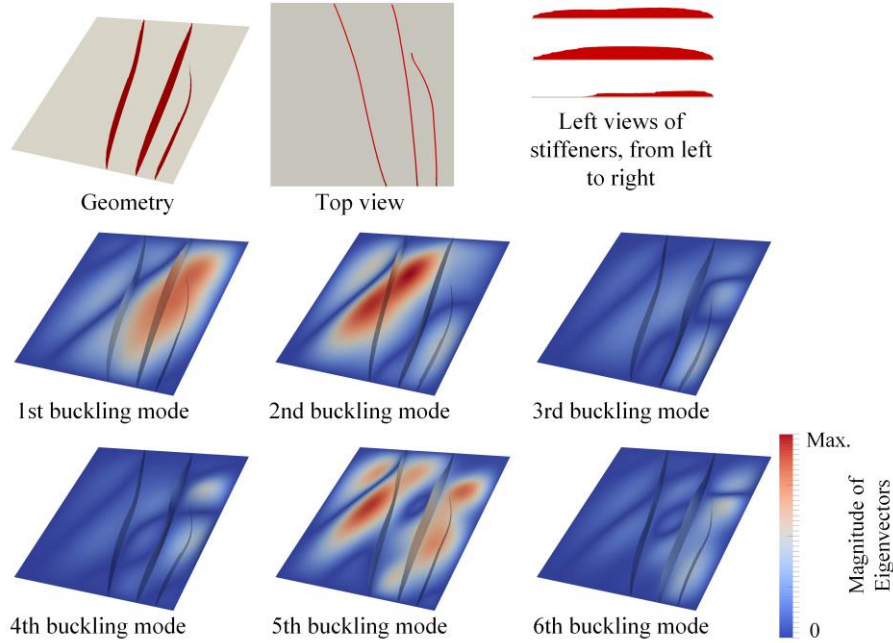


Fig. 20: Optimized design considering initial design with 7 vertical stiffeners, $m = 0.563$ kg, and its first 6 buckling modes under shear loading, $\lambda_1 = 1.000$, $\lambda_2 = 1.060$, $\lambda_3 = 1.094$, $\lambda_4 = 1.119$, $\lambda_5 = 1.210$, $\lambda_6 = 1.242$.

The optimized design is shown in Fig. 20. Its mass is 0.563 kg. The mass constraint is satisfied. The stiffener layout is optimized, and the redundant material is removed. The comparison of the geometries of the optimized design in this optimization problem and the one obtained by mass minimization with a buckling constraint in Fig. 11 is given in Fig. 21. It can be seen that both the topology and layout of the two results are almost same. However, there are minor differences in the stiffener curves and stiffener heights causing the buckling load factors in Fig. 11 to be a little larger (within 3%) than the ones in Fig. 20. It is noted that, since both the topology optimization problems of mass minimization with buckling constraint and critical buckling load factor maximization with mass constraint are highly nonlinear, many local optima exist. Therefore, the similarity between the results in Figs. 11 and 20 demonstrates that the optimization methodology proposed in this paper show a reasonable level of reliability.

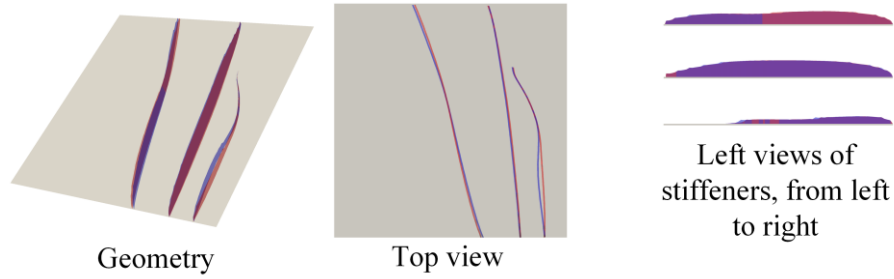


Fig. 21: Comparison of the geometries of the optimized designs in Figs. 11 (blue, $m = 0.563$ kg and $\lambda_1 = 1.008$) and 20 (red, $m = 0.563$ kg and $\lambda_1 = 1.000$).

An optimization in which the layout design variables are excluded is also performed. The initial design with 7 vertical stiffeners shown in Fig. 10 is used. The result is presented in Fig. 22. Compared with the optimized design in Fig. 20 with simultaneous layout and topology optimization, the optimized design in Fig. 22 with topology optimization only, has a worse buckling performance. There is a 30.9% difference in the critical buckling load factors. This shows the simultaneous layout and topology optimization can be effective in improving the buckling performance.

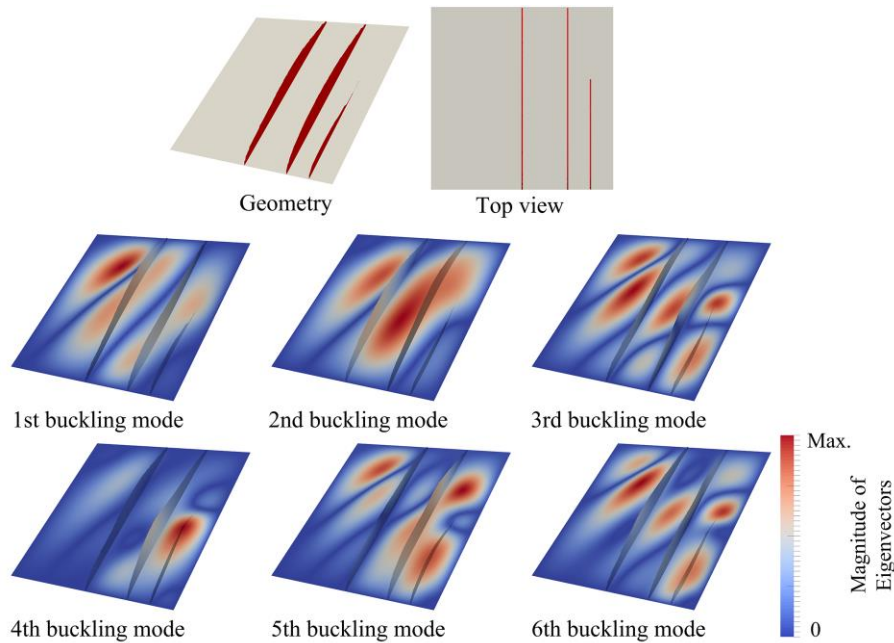


Fig. 22: Optimized design without the layout optimization, considering initial design with 7 vertical stiffeners, $m = 0.563$ kg, and its first 6 buckling modes under shear loading, $\lambda_1 = 0.691$, $\lambda_2 = 0.717$, $\lambda_3 = 0.805$, $\lambda_4 = 0.823$, $\lambda_5 = 0.884$, $\lambda_6 = 0.958$.

V. Conclusion

This paper presents a new level-set-based method for simultaneous layout and topology optimization of curved stiffened panels. To the best of the authors' knowledge, this paper is the first to investigate the simultaneous layout and topology optimization of stiffened panels with a gradient-based approach. The construction and update of the geometry and finite element models using the level set method and a free-form mesh deformation method are described in detail. Both the problems of mass minimization with buckling constraint and critical buckling load factor maximization with mass constraint are studied. A sensitivity analysis is presented, and the optimization algorithm is outlined. The numerical results show the presented method is able to efficiently solve the two stiffened panel design problems. The stiffener layout is optimized, the redundant stiffeners are removed, and the material in the remaining stiffeners is redistributed to satisfy all the constraints. For the buckling-constrained problem, when the p -norm function and the gradient-based optimizer IPOPT are used, the presented method is able to satisfy the buckling constraints with an adaptive scaling method.

New manufacturing techniques, such as additive manufacturing, are making it possible to fabricate complex designs such as the curved stiffened panels. However, to guarantee the manufacturability of these optimized designs, some manufacturing constraints, such as the heights and turning radii of the stiffeners, should also be taken into account.

Acknowledgments

The authors acknowledge the support from the Engineering and Physical Sciences Research Council Fellowship for Growth, EP/M002322/2. We would also like to thank the Numerical Analysis Group at the Rutherford Appleton Laboratory for their FORTRAN HSL packages (HSL, a collection of Fortran codes for large-scale scientific computation. See <http://www.hsl.rl.ac.uk/>).

References

- [1] Bedair, O. K. "Influence of stiffener location on the stability of stiffened plates under compression and in-plane bending," *International journal of mechanical sciences* Vol. 39, No. 1, 1997, pp. 33-49.

doi: [https://doi.org/10.1016/0020-7403\(96\)00017-3](https://doi.org/10.1016/0020-7403(96)00017-3)

- [2] Lamberti, L., Venkataraman, S., Haftka, R. T., and Johnson, T. F. "Preliminary design optimization of stiffened panels using approximate analysis models," *International journal for numerical methods in engineering* Vol. 57, No. 10, 2003, pp. 1351-1380.
doi: <https://doi.org/10.1002/nme.781>
- [3] Kapania, R., Li, J., and Kapoor, H. "Optimal design of unitized panels with curvilinear stiffeners," *AIAA 5th ATIO and 16th Lighter-Than-Air Sys Tech. and Balloon Systems Conferences*. 2005, p. 7482.
doi: <https://doi.org/10.2514/6.2005-7482>
- [4] Colson, B., Bruyneel, M., Grihon, S., Raick, C., and Remouchamps, A. "Optimization methods for advanced design of aircraft panels: a comparison," *Optimization and Engineering* Vol. 11, No. 4, 2010, pp. 583-596.
doi: <https://doi.org/10.1007/s11081-008-9077-8>
- [5] Bhatia, M., Kapania, R. K., and Evans, D. "Comparative study on optimal stiffener placement for curvilinearly stiffened panels," *Journal of Aircraft* Vol. 48, No. 1, 2011, pp. 77-91.
doi: <https://doi.org/10.2514/1.C000234>
- [6] Mulani, S. B., Slemple, W. C., and Kapania, R. K. "EBF3PanelOpt: An optimization framework for curvilinear blade-stiffened panels," *Thin-Walled Structures* Vol. 63, 2013, pp. 13-26.
doi: <https://doi.org/10.1016/j.tws.2012.09.008>
- [7] Tamijani, A. Y., Mulani, S. B., and Kapania, R. K. "A framework combining meshfree analysis and adaptive kriging for optimization of stiffened panels," *Structural and Multidisciplinary Optimization* Vol. 49, No. 4, 2014, pp. 577-594.
doi: <https://doi.org/10.1007/s00158-013-0993-7>
- [8] Chu, S., Yang, Z., Xiao, M., Qiu, H., Gao, K., and Gao, L. "Explicit topology optimization of novel polyline-based core sandwich structures using surrogate-assisted evolutionary algorithm," *Computer Methods in Applied Mechanics and Engineering* Vol. 369, 2020, p. 113215.
doi: <https://doi.org/10.1016/j.cma.2020.113215>
- [9] Stanford, B. K., Jutte, C. V., and Coker, C. A. "Aeroelastic Sizing and Layout Design of a Wingbox Through Nested Optimization," *AIAA Journal* Vol. 57, No. 2, 2019, pp. 848-857.
doi: <https://doi.org/10.2514/1.J057428>

- [10] Bendsøe, M. P., and Kikuchi, N. "Generating optimal topologies in structural design using a homogenization method," *Computer methods in applied mechanics and engineering* Vol. 71, No. 2, 1988, pp. 197-224.
doi: [https://doi.org/10.1016/0045-7825\(88\)90086-2](https://doi.org/10.1016/0045-7825(88)90086-2)
- [11] Bendsøe, M. P. "Optimal shape design as a material distribution problem," *Structural optimization* Vol. 1, No. 4, 1989, pp. 193-202.
doi: <https://doi.org/10.1007/BF01650949>
- [12] Sigmund, O. "A 99 line topology optimization code written in Matlab," *Structural and multidisciplinary optimization* Vol. 21, No. 2, 2001, pp. 120-127.
doi: <https://doi.org/10.1007/s001580050176>
- [13] Andreassen, E., Clausen, A., Schevenels, M., Lazarov, B. S., and Sigmund, O. "Efficient topology optimization in MATLAB using 88 lines of code," *Structural and Multidisciplinary Optimization* Vol. 43, No. 1, 2011, pp. 1-16.
doi: <https://doi.org/10.1007/s00158-010-0594-7>
- [14] Wang, M. Y., Wang, X., and Guo, D. "A level set method for structural topology optimization," *Computer methods in applied mechanics and engineering* Vol. 192, No. 1-2, 2003, pp. 227-246.
doi: [https://doi.org/10.1016/S0045-7825\(02\)00559-5](https://doi.org/10.1016/S0045-7825(02)00559-5)
- [15] Allaire, G., Jouve, F., and Toader, A.-M. "Structural optimization using sensitivity analysis and a level-set method," *Journal of computational physics* Vol. 194, No. 1, 2004, pp. 363-393.
doi: <https://doi.org/10.1016/j.jcp.2003.09.032>
- [16] Sethian, J. A., and Wiegmann, A. "Structural boundary design via level set and immersed interface methods," *Journal of computational physics* Vol. 163, No. 2, 2000, pp. 489-528.
doi: <https://doi.org/10.1006/jcph.2000.6581>
- [17] Dunning, P. D., and Kim, H. A. "Introducing the sequential linear programming level-set method for topology optimization," *Structural and Multidisciplinary Optimization* Vol. 51, No. 3, 2015, pp. 631-643.
doi: <https://doi.org/10.1007/s00158-014-1174-z>
- [18] Xie, Y. M., and Steven, G. P. "A simple evolutionary procedure for structural optimization," *Computers & structures* Vol. 49, No. 5, 1993, pp. 885-896.
doi: [https://doi.org/10.1016/0045-7949\(93\)90035-C](https://doi.org/10.1016/0045-7949(93)90035-C)

- [19] Huang, X., and Xie, M., *Evolutionary topology optimization of continuum structures: methods and applications*: John Wiley & Sons, 2010.
- [20] Neves, M. M., Sigmund, O., and Bendsøe, M. P. "Topology optimization of periodic microstructures with a penalization of highly localized buckling modes," *International Journal for Numerical Methods in Engineering* Vol. 54, No. 6, 2002, pp. 809-834.
doi: <https://doi.org/10.1002/nme.449>
- [21] Dunning, P. D., Ovtchinnikov, E., Scott, J., and Kim, H. A. "Level-set topology optimization with many linear buckling constraints using an efficient and robust eigensolver," *International Journal for Numerical Methods in Engineering* Vol. 107, No. 12, 2016, pp. 1029-1053.
doi: <https://doi.org/10.1002/nme.5203>
- [22] Gao, X., and Ma, H. "Topology optimization of continuum structures under buckling constraints," *Computers & Structures* Vol. 157, 2015, pp. 142-152.
doi: <https://doi.org/10.1016/j.compstruc.2015.05.020>
- [23] Thomsen, C. R., Wang, F., and Sigmund, O. "Buckling strength topology optimization of 2D periodic materials based on linearized bifurcation analysis," *Computer Methods in Applied Mechanics and Engineering* Vol. 339, 2018, pp. 115-136.
doi: <https://doi.org/10.1016/j.cma.2018.04.031>
- [24] Townsend, S., and Kim, H. A. "A level set topology optimization method for the buckling of shell structures," *Structural and Multidisciplinary Optimization* Vol. 60, No. 5, 2019, pp. 1783-1800.
doi: <https://doi.org/10.1007/s00158-019-02374-9>
- [25] Bruyneel, M., Colson, B., and Remouchamps, A. "Discussion on some convergence problems in buckling optimisation," *Structural and Multidisciplinary Optimization* Vol. 35, No. 2, 2008, pp. 181-186.
doi: <https://doi.org/10.1007/s00158-007-0129-z>
- [26] Dienemann, R., Schumacher, A., and Fiebig, S. "Considering Linear Buckling for 3D Density Based Topology Optimization," *International Conference on Engineering Optimization*. Springer, 2018, pp. 394-406.
doi: https://doi.org/10.1007/978-3-319-97773-7_36
- [27] Ferrari, F., and Sigmund, O. "Revisiting topology optimization with buckling constraints," *Structural and Multidisciplinary Optimization* Vol. 59, No. 5, 2019, pp. 1401-1415.

doi: <https://doi.org/10.1007/s00158-019-02253-3>

[28] Stanford, B., Beran, P., and Bhatia, M. "Aeroelastic topology optimization of blade-stiffened panels," *Journal of Aircraft* Vol. 51, No. 3, 2014, pp. 938-944.

doi: <https://doi.org/10.2514/1.C032500>

[29] Gurav, S., and Kapania, R. "Development of framework for the design optimization of unitized structures," *50th AIAA/ASME/ASCE/AHS/ASC Structures, Structural Dynamics, and Materials Conference 17th AIAA/ASME/AHS Adaptive Structures Conference 11th AIAA No.* 2009, p. 2186.

doi: <https://doi.org/10.2514/6.2009-2186>

[30] Sethian, J. A., *Level set methods and fast marching methods: evolving interfaces in computational geometry, fluid mechanics, computer vision, and materials science*: Cambridge university press, 1999.

[31] Osher, S., Fedkiw, R., and Piechor, K. "Level set methods and dynamic implicit surfaces." American Society of Mechanical Engineers Digital Collection, 2004.

doi: <https://doi.org/10.1115/1.1760521>

[32] Wächter, A., and Biegler, L. T. "On the implementation of an interior-point filter line-search algorithm for large-scale nonlinear programming," *Mathematical programming* Vol. 106, No. 1, 2006, pp. 25-57.

doi: <https://doi.org/10.1007/s10107-004-0559-y>

[33] Jiang, G.-S., and Peng, D. "Weighted ENO schemes for Hamilton--Jacobi equations," *SIAM Journal on Scientific computing* Vol. 21, No. 6, 2000, pp. 2126-2143.

doi: <https://doi.org/10.1137/S106482759732455X>

[34] Bathe, K. J., and Dvorkin, E. N. "A four-node plate bending element based on Mindlin/Reissner plate theory and a mixed interpolation," *International Journal for Numerical Methods in Engineering* Vol. 21, No. 2, 1985, pp. 367-383.

doi: <https://doi.org/10.1002/nme.1620210213>

[35] Chapelle, D., and Bathe, K.-J., *The finite element analysis of shells-fundamentals*: Springer Science & Business Media, 2010.

[36] Sederberg, T. W., and Parry, S. R. "Free-form deformation of solid geometric models," *ACM SIGGRAPH computer graphics* Vol. 20, No. 4, 1986, pp. 151-160.

doi: <https://doi.org/10.1145/15886.15903>

- [37] HSL, H., *A collection of Fortran codes for large scale scientific computation*, 2002, 2002.
- [38] Lehoucq, R. B., Sorensen, D. C., and Yang, C., *ARPACK users' guide: solution of large-scale eigenvalue problems with implicitly restarted Arnoldi methods*: SIAM, 1998.
- [39] Picelli, R., Townsend, S., Brampton, C., Norato, J., and Kim, H. "Stress-based shape and topology optimization with the level set method," *Computer methods in applied mechanics and engineering* Vol. 329, 2018, pp. 1-23.
doi: <https://doi.org/10.1016/j.cma.2017.09.001>
- [40] Choi, K. K., and Kim, N.-H., *Structural sensitivity analysis and optimization 1: linear systems*: Springer Science & Business Media, 2004.
- [41] Adalsteinsson, D., and Sethian, J. A. "The fast construction of extension velocities in level set methods," *Journal of Computational Physics* Vol. 148, No. 1, 1999, pp. 2-22.
doi: <https://doi.org/10.1006/jcph.1998.6090>
- [42] Le, C., Norato, J., Bruns, T., Ha, C., and Tortorelli, D. "Stress-based topology optimization for continua," *Structural and Multidisciplinary Optimization* Vol. 41, No. 4, 2010, pp. 605-620.
doi: <https://doi.org/10.1007/s00158-009-0440-y>